Nanoscale

Accepted Manuscript

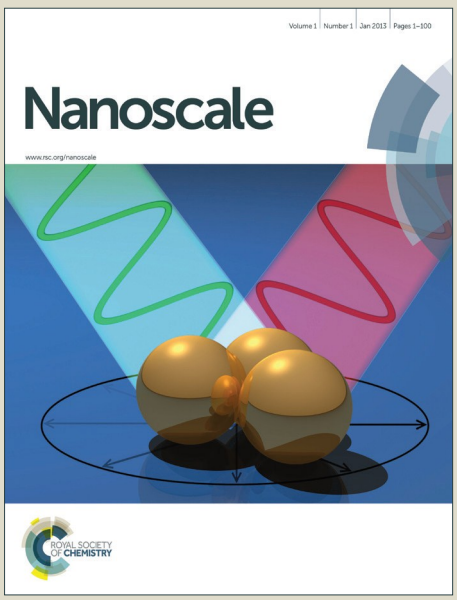

ROYAL SOCIETY OF CHEMISTRY

www.rsc.org/nanoscale

Journal Name

ARTICLE TYPE

Cite this: DOI: 10.1039/xxxxxxxxxx

Reactive wetting properties of TiO_2 nanoparticles predicted by *ab initio* molecular dynamics simulations†

Erik G. Brandt,[a] Lorenzo Agosta,[a] and Alexander P. Lyubartsev[a]*

Received Date
Accepted Date

DOI: 10.1039/xxxxxxxxxx

www.rsc.org/journalname

Small-sized wet TiO_2 nanoparticles have been investigated by *ab initio* molecular dynamics simulations. Chemical and physical adsorption of water on the TiO_2-water interface was studied as function of the water content, ranging from dry nanoparticles to wet nanoparticles with monolayer coverage of water. The surface reactivity was shown to be a concave function of the water content and driven by surface defects. The local coordination number at the defect was identified as the key factor to whether water adsorption proceeds through dissociation or physisorption on the surface. A consistent picture of TiO_2 nanoparticle wetting at the microscopic level emerges, that corroborate existing experimental data and gain further insight into the molecular mechanisms behind nanoparticle wetting. These calculations will facilitate the engineering of metal oxide nanoparticles with controlled catalytic water activity.

Introduction

Solids are often covered by thin water films which determine their interactions with surrounding matter. Ever since the capability to use titanium dioxide (TiO_2) for hydrogen gas production from water was discovered,[1] and the efficiency boost provided by dye-sensitized solar cells was revealed,[2] both dry and wet TiO_2 surfaces have drawn great interest from the scientific community.[3] Applications taking advantage of the nanoproperties of the TiO_2-water interface are numerous in modern technology (e.g., in solar cells,[4] in self-cleaning materials,[5] during photocatalysis[6,7]), but concerns have also been raised over the potential health hazards linked to the use of nano-TiO_2 in consumer products.[8,9] TiO_2 nanoparticles (NPs) of size 1 to 100 nm are particularly interesting for biomedical applications.[10] Due to their small sizes, they may reach previously inaccessible parts of the body (e.g. by crossing the blood-brain barrier[11]) and be suitable for targeted drug delivery[12] and medical implants,[13] since their high surface-to-bulk ratio give them properties in remarkable contrast to their bulk counterparts. Microscopic understanding of water reactivity and wetting of nanosized TiO_2 is therefore crucial to understand nanotoxicity,[14] to control photocatalyticity,[15,16] and for using interfacial water[17] to modulate adsorption of biomolecules such as proteins, lipids and sugars[18] to metal oxide nanoparticles.

Many aspects of the structure and dynamics of the TiO_2-water interface are still unclear. These include whether water dissociates on defect-free TiO_2 surfaces,[19] the orientation and bond lengths of adsorbed waters,[20] indirect participation of subsurface oxygen vacancies during water dissociation,[21] and the roles of particle morphology and size in photocatalytic activity of nano-TiO_2 (see the references in Ref. 22). On flat surfaces, experiments[20,23–26] and theoretical calculations[27–31] suggest that interfacial waters complete the coordination sphere of surface titanium atoms either by molecular adsorption or by dissociation (the redundant proton hops to a neighbor "bridging" 2-fold coordinated oxygen[25]). Much less is known about the irregular surfaces of wet nanoparticles, where the higher frequency of surface defects may lead to higher reactivity.[32,33] For example, Zhang *et al.*[34] found low Ti coordination numbers (5.1 vs. 6 for bulk) for small-sized (2 nm) amorphous nanoparticles using synchrotron wide-angle x-ray scattering (WAXS) and molecular modeling. To further complicate matters, TiO_2 exists in three forms (polymorphs) with distinct properties: rutile, anatase and brookite.[35] The most stable bulk phase is rutile, followed by anatase and then brookite. The stability chain is shuffled in the nano world; anatase becomes more stable than rutile when the particle size drops below ~ 140 Å.[36] Overall, the polymorphic basis of hydrophobic/hydrophilic adsorption behavior[37] and photocatalytic activity[38] of nano-TiO_2 remains unsatisfactorily obscured.

Theoretical calculations have addressed some controversies of

[a] *Department of Materials and Environmental Chemistry, Stockholm University, Stockholm, Sweden*

* *Corresponding author. E-mail:alexander.lyubartsev@mmk.su.se*

† Electronic Supplementary Information (ESI) available: Simulation data on equilibration of energies and structures (root-mean-square-deviations and coordination numbers); radial distribution functions for all O–Ti pairs over the entire data domain; comparison of coordination number distributions for dry and wet nanoparticles; dynamics of water reactivity; high-resolution electron density for the rutile NP. A movie of the simulation trajectory for the rutile $(TiO_2)_{24}{\cdot}30H_2O$ system. See DOI: 10.1039/b000000x/

the TiO_2–water interface of planar surfaces[39,40] and nanoparticles[22] (and also the interface with organic molecules,[41,42] relevant to solar cell applications[43]). The majority of simulation work on inorganic nanoparticles[44] have either employed classical molecular dynamics on larger nanoparticles[45,46] or structure optimizations of single configurations,[47] typically in the absence of water.[48,49] Only recently has the increased availability of computer power allowed *ab initio* simulations with realistic dynamics computed from density functional theory.[50] Liu *et al.*[29] provided the first *ab initio* simulations of rutile slabs with full monolayer coverage, showing that water dissociation is not favored (by the small amount $\Delta E \sim 0.1$ eV) on defect-free TiO_2(100) rutile.

To the best of our knowledge, the present work is the first *ab initio* simulations of small-sized TiO_2 nanoparticles in contact with water. For the first time, we can study the real-time dynamics of the splitting of water molecules at the surface from first principles, and show how surface defects and their coordination numbers determine the equilibrium surface structure. Altogether, we provide an atomistic description of the water adsorption mechanism on nano-TiO_2 that explains experimental data.[32] We simulate the TiO_2–water interface up to monolayer wetting with respect to the baseline case of dry nanoparticles. First, we describe the nanoparticles' structures and how they are influenced by wetting, to what extent morphologies come into play, and relations to their bulk counterparts. Then, we investigate the surface energetics of the wet nanoparticles versus the dry nanoparticles. We proceed by describing the surface structure in terms of surface groups and use this analysis to identify adsorption sites from radial distribution functions. The water reactivity is quantified in terms of coordination numbers and degree of dissociation. State-of-the-art analysis of high-resolution electron densities confirm the amount of charge transfer occurring at the surface. Finally, an atomically detailed explanation of the hydration mechanisms is given to explain recent XPS experimental data of wet nanoparticles.[32]

Results and discussion

The aim of this work is to clarify the interfacial structure during wetting of small-sized TiO_2 nanoparticles.[32] Questions to answer are: (1) What role does morphology play in wetting at the nanoscale? (2) How reactive are small-sized TiO_2 nanoparticles and how does the catalytic activity depend on water content? (3) What are the major adsorption pathways when water adsorbs on small-sized TiO_2 nanoparticles? (4) How much does the NP surface atoms rearrange to accommodate for the solvation layer and is charge transfer and polarization important to understand the TiO_2–water complex?

To answer these questions, we performed *ab initio* molecular dynamics simulations (AIMD) of wet titanium dioxide nanoparticles (TiO_2 NPs), with stoichiometry $(TiO_2)_{24}{\cdot}nH_2O$, at 37 °C ($T = 310$ K). Here, $n = \{0,1,3,8,15,30\}$ is the number of water molecules. The role of morphology for wetting at the nanoscale was determined by cutting NPs out of the unit cells of the three bulk phases of TiO_2; rutile (tetragonal with space group $P4_2/mnm$), anatase (tetragonal with space group $Pcab$) and brookite (orthorhombic with space group $I4_1/amd$). These model

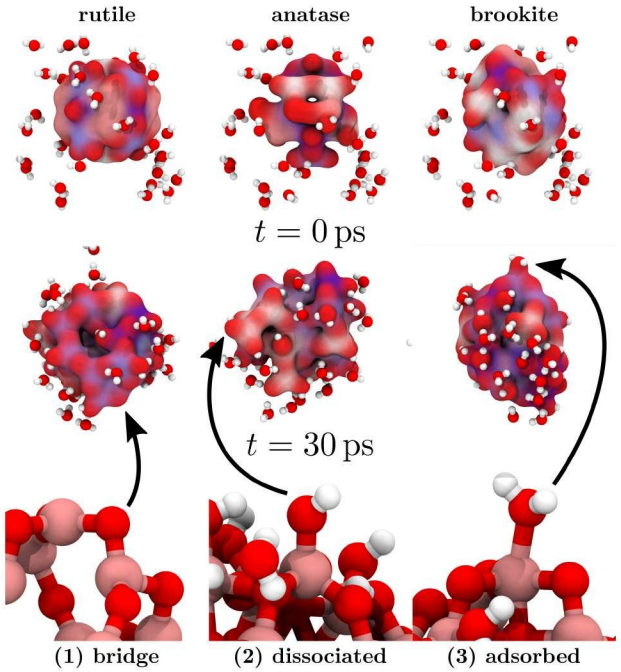

Fig. 1 The initial (top panels, $t = 0$ ps) and final (middle panels, $t = 30$ ps) configurations of the systems with the highest degree of wetting ($n = 30$ water molecules). The labels over the top panels refer to the TiO_2 polymorph corresponding to each initial structure. Ti and O atoms that are at least 1-fold coordinated belong to the nanoparticle and are drawn with surface representations. The color coding is based on coordination numbers, and ranges from red (lowest, oxygens) via white (intermediate) to blue (highest, titaniums). Water oxygens (0-fold coordinated) and hydrogens are drawn with ball-and-stick representations. Representative surface structures from the final configurations are shown in the bottom panel: (1) 2-fold coordinated oxygen bridges on the surface, (2) OH–group from dissociated water, and (3) molecularly adsorbed water molecule. The last two occurs at defects on the TiO_2 nanoparticle surface.

nanoparticles are approximately spherical, of sizes ~ 1 nm, and represent the smallest particles with the features of the corresponding bulk structures (as studied systematically in the rutile case[51–53]). The wetting in the simulations was varied from dry NPs ($n = 0$) to monolayer surface coverage at 0.08 Å^{-2} ($n = 30$, which is in practice slightly below monolayer coverage due to the inhomogeneous distribution of adsorbed water molecules on the NPs' surfaces). Fig. 1 shows the initial crystalline structures (top panels), and the final configurations (middle panels) after 30 ps of simulation time of the systems with monolayer wetting. A movie of the simulation trajectory of the rutile $(TiO_2)_{24}{\cdot}30H_2O$ system is provided for reference as ESI. More details on how the simulations were set up and performed are found in the Methods Section and in the ESI. The NPs maintain their approximately spherical shapes throughout the simulations (although the brookite NP is slightly elongated) at all hydration levels. Visual inspection of the equilibrated configurations shows that surface defects are more homogeneously distributed over the surface of the rutile and anatase NPs compared to the brookite NP. At the highest wetting (comparable to monolayer coverage) this can be seen from water molecules adsorbing more homogeneously on the rutile and anatase NPs, but cluster on the brookite nanoparticle.

We now present a careful analysis of our simulations to reveal the atomic structure of the interfacial water on nanosized TiO_2 NPs.

Atomic structure of wet TiO_2 nanoparticles

We quantify nanoparticle morphology by calculating root-mean-square deviations (RMSDs), Ti−O−Ti and O−Ti−O angle distributions, radial distribution functions (RDFs) between elements, and coordination numbers (CNs) for each element in the nanoparticles. The results from dry ($n = 0$) and wet ($n = 30$) nanoparticles are compared to find the impact on hydration structure of small-sized nanoparticles based on morphology.

Fig. 2 shows the root-mean-square deviation (RMSD) in the wet systems, which stabilize within 5 ps of simulated time, after which no further increase is found. Each nanoparticle simulation is compared to its initial structure and to the other two polymorphs. The RMSDs are a factor of three lower (5 to 5.5 Å compared to 1.5 to 2 Å) for the same morphology as compared to the others. Almost identical RMSDs were found at all levels of wetting (see Fig. **??** in the ESI), which demonstrates that the nanoparticles' structures are retained independently of the wetting, except for surface reorganization due to water reactivity as discussed later. The curves in Fig. 2 can be grouped into one low-RMSD and one high-RMSD set of curves. The first group corresponds to nanoparticles compared to their initial polymorph, and the second group corresponds to nanoparticles compared to the two other polymorphs. The RMSD differences within each group are small (1.5 to 2 Å and 5 to 5.5 Å, respectively) and shows that no polymorph is closer to their ideal crystal structure than the others. The equilibrium structure of the nanoparticle is intermediate between the bulk morphology (corresponding to zero RMSD) and an amorphous phase (corresponding to RMSD independent of starting structure). Clearly, morphology is less defined at the nanoscale.

To further quantify the atomic structures, we calculated the angle distributions of ∠Ti−O−Ti and ∠O−Ti−O within the dry and wet nanoparticles and compared them to bulk crystals (water oxygens were excluded from the calculations, as explained in the Methods section). They are shown in Fig. 3, where the bulk angles and corresponding intensities are drawn with vertical lines. The angle distributions for dry and wet NPs are similar and considerably broadened compared to the sharp lines found in the crystal structures. The onset of bulk behavior in TiO_2 NPs is not accurately known, but at least 1000 molecular TiO_2 units are required because of the covalent nature of the Ti−O bond.[54] Such system sizes are outside the reach of current *ab initio* molecular dynamics simulations. The $(TiO_2)_{24}{\cdot}nH_2O$ cluster is therefore too small to exhibit the true morphologies of bulk TiO_2. Fig. 3 shows that ∠O−Ti−O is in fair agreement with the crystal structures but with a broad distribution. The 99°-peak is accentuated while the 130°-peak is suppressed in the ∠Ti−O−Ti-distribution of the anatase and brookite simulations. Overall, we find angle distributions like the experimental crystal structures, although the 154°-peak of the O−Ti−O-distribution in the anatase simulation is skewed to 135°.

Fig. 4 shows the ∠H−O−H- and ∠Ti−O−H-distributions (water and surface OH-groups). The average water angle is 105.3° in excellent agreement to the experimental geometry.[55] The average of the ∠Ti−O−H-distributions was $(118.1 \pm 12.0)°$. No significant difference was found between the polymorphs. The broader ∠Ti−O−H-distribution (as compared to the ∠H−O−H-distribution) demonstrates pronounced fluctuations in orientation of surface hydroxyls while waters are less flexible. Oxygens behaved in the same way when coordinated to one hydrogen (OH−group) or two or more hydrogens (molecularly adsorbed, data not shown). The Ti−O−H angle is independent of molecular adsorption or dissociation.

Radial distribution functions (RDFs) between differently coordinated elements (see Methods section) were computed to define the local ordering in the dry ($n = 0$) and wet ($n = 30$) $(TiO_2)_{24}{\cdot}nH_2O$ nanoparticles. Fig. 5 shows the RDF for O−Ti pairs in the range 1 to 3 Å. This first RDF peak corresponds to the O−Ti bond distance and integrates to the nearest-neighbor coordination number. The RDFs of all pairs of elements (between Ti, O and H) over the entire r domain are given in the Fig. **??** in the ESI. Fig. 5 shows a single peak at 1.87 Å in $g_{\mathrm{OTi}}(r)$ between 1 to 3 Å for wet nanoparticles, but two peaks (at 1.65 Å and 1.87 Å) in the same range for dry nanoparticles. The additional peak is most pronounced in the rutile and anatase simulations.

We performed an in-depth analysis based on coordination number O−Ti RDFs which gives a unique fingerprint of each surface structure. Fig. 6 shows $g_{\mathrm{O}_n\mathrm{Ti}_m}(r)$: the RDF between n-fold coordinated oxygens and m-fold coordinated titaniums. The top panels in Fig. 6 correspond to dry nanoparticles and the bottom panels correspond to wet nanoparticles. The major contribution to these RDFs are from 2- and 3-fold coordinated oxygens to 4- (dry nanoparticles) and 5-fold (wet nanoparticles) coordinated titaniums. The Ti_4-contribution is dominant for the dry NPs while the Ti_5-contribution is prominent for the wet NPs. The O−Ti bond is in the range 1.6 to 2.2 Å and increases with the coordination number (CN).

The distributions for 2- and 3-fold coordinated oxygens are single-peaked and alike for dry and wet nanoparticles, since the core structures of the NPs are intact during the simulations. Comparing Fig. 6 to Fig. 5 proves that the dry NP-peak at 1.65 Å is due to 1-fold coordinated surface oxygens which are protonated after wetting. The coordination number-based RDFs conclusively show that the single O_1-Ti_n peak of the dry NPs (red lines in upper panels of Fig. 6) is split to three peaks for the wet nanoparticles (red lines in lower panels of Fig. 6). $g_{\mathrm{O_1Ti}}(r)$ in Fig. 7 further reveals three distinct O−Ti bond distances depending on whether O_1 is coordinated to Ti_4, Ti_5, or Ti_6.

Each peak corresponds to O_1 having zero hydrogens (deprotonated Ti−O surface bond), one hydrogen (Ti−OH surface group) or two hydrogens (Ti−OH_2, adsorbed water molecule). The O−Ti bond distance increases with the number of hydrogens, from 1.68 Å for Ti−O, to 1.83 Å for Ti−OH, and finally to 2.15 Å (2.2 Å for brookite) for Ti−OH_2. From the O−Ti coordination number distributions (see Fig. 9, and the following discussion in the text) we find that 90 % of the O_1 atoms are protonated by either one or two hydrogens. Ti_4 atoms are terminated with O_1-

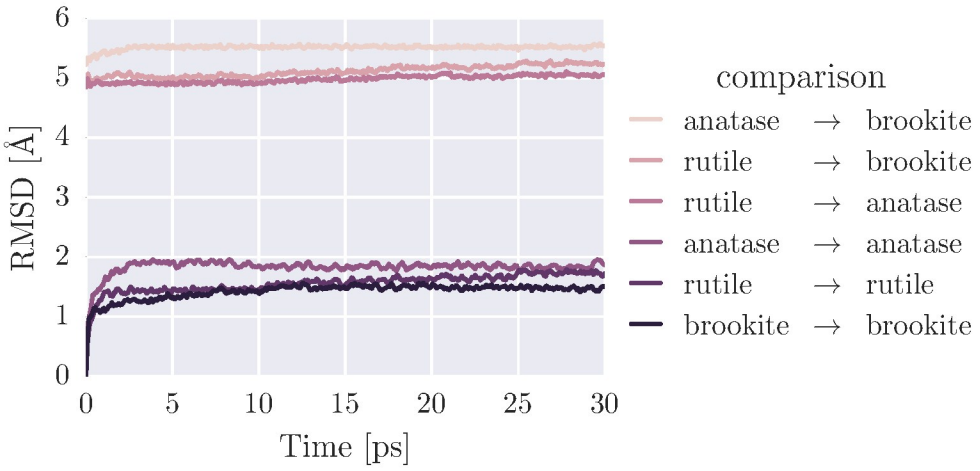

Fig. 2 Root-mean-square deviations (RMSDs) for the simulated system with respect to the initial structures of the nanoclusters of the TiO_2 polymorphs. The RMSDs stabilize after 5 ps of simulation time. The RMSDs are a factor of 3 lower when systems are compared to their starting structures rather than to the other two polymorphs.

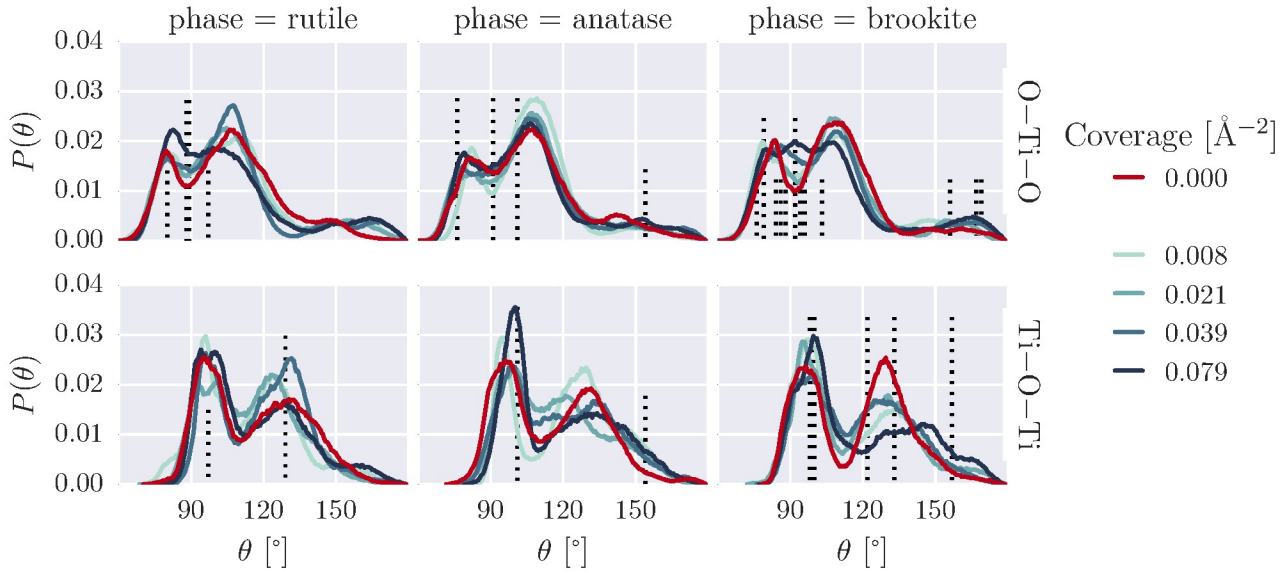

Fig. 3 Angle distributions for $\angle$O−Ti−O (top panels) and $\angle$Ti−O−Ti (bottom panels) in the simulated systems, comparing nanoparticles with different coverages (0 to 0.08 Å^{-2}). The dotted vertical lines mark the unit cell angles of the respective TiO_2 morphologies and are scaled with the maximum of the simulated distributions.

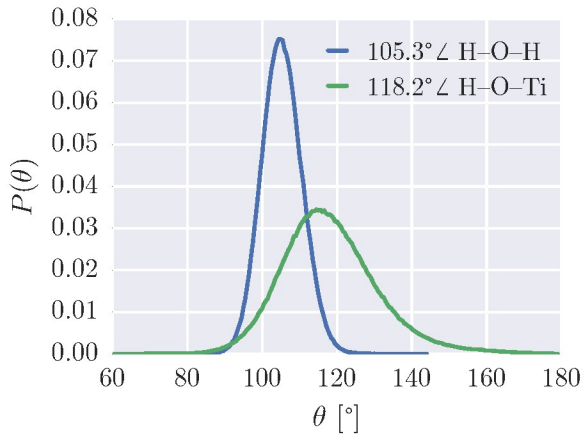

Fig. 4 Angle distributions for ∠H−O−H (water) and ∠H−O−Ti (surface OH−groups). The water angle was the same in all polymorph simulations. The H−O−Ti angle distribution was averaged over the polymorphs and different surface coverages, since the variations were smaller than the statistical uncertainty of the simulations.

and O_1H-groups but never with molecularly adsorbed water. Ti_5 is evenly distributed between either water dissociation in form of OH-groups or molecularly adsorbed OH_2-surface termination. The Ti−OH_2 bond is 2.15 Å. This longer distance implies a weaker bond by physisorption and is in agreement with (2.21 ± 0.02) Å, which is the adsorption bond length identified by photoelectron diffraction for molecularly adsorbed water on the rutile (110) surface.[20]

Previous AIMD simulations of fully hydrated TiO_2(110) slabs unambiguously reported molecular adsorption on defect-free surfaces.[29] The bond distance was calculated to be 2.1 Å, i.e., 0.1 Å smaller than the experimental value.[20] We note that the extent of water dissociation on rutile (110) is vividly debated in the literature (see e.g. Refs. 24,27–29 and the references therein), and theoretical results are sensitive to the exchange-correlation functional employed at the generalized gradient approximation (GGA) level of theory.[27] The O_1−Ti_6 bond in Fig. 7 corresponds to the molecular adsorption site "on top of 5-fold coordinated surface titaniums on rutile (110) ",[20] since we include the adsorbed atom in the total coordination number. We find this bond distance to be ~ 2.2 Å, in excellent agreement to the experimental value (2.21 Å).

Finally, we remark that the distributions of 2- and 3-fold coordinated oxygens in Fig. 6 are single-peaked but broad and somewhat skewed, which reflects the amorphous element to the atomic structure. Then, we have the following classification of O−Ti bonds in the NPs: (1) Deprotonated, 1-fold coordinated surface oxygens at 1.68 Å, (2) surface oxygens (OH-groups or oxygen bridges) at 1.85 Å and (3) bulk-like oxygens broadly distributed from 1.9 to 2.0 Å. The specific numbers 1.94 Å (rutile), 1.95 Å (anatase) and 1.92 Å (brookite) are to be compared to the corresponding bonds in the crystal structure: 1.96 Å (rutile), 1.946 Å (anatase), and the six different bond lengths in brookite between 1.87 to 2.04 Å, see Refs. 56,57. It suffices here to say that the values computed from our simulations are in satisfactory agreement with the experimental values given the distorted structures of the small-sized nanoparticles compared to their bulk counterparts. The largest bond distance, 2.2 Å is found for molecularly adsorbed water molecules on the nanoparticle surface. Such waters adsorb to Ti defects (rather than dissociating) on the surface in the absence of adjacent bridging oxygens.

Surface energetics of wet nanoparticles

We monitored the potential energy during the simulations, and found that the nanoparticles relax towards structures described partly as amorphous, and partly as bulk structures. The initial atomic rearrangement takes place within the first 1 to 2 ps of simulation time (see Fig. **??** and **??** in the ESI). Next, the energies of the wet nanoparticles slowly decrease as water adsorbs on the surface before leveling off after 15 ps of simulated time, which coincides with the water reactivity equilibration time (see Fig. **??** in the ESI). The dry nanoparticles are more difficult to equilibrate than the wet nanoparticles since adsorbed water molecules lower the surface energies of the wet NPs. The dry NPs need to rely on surface reorganization which is slower.

The adsorption enthalpy $\Delta h_{\mathrm{ads}}(n)$ as a function of the n number of water molecules on the surface is a measure of the NPs' water binding strength. It is calculated from simulations by

$$\begin{aligned}\Delta h_{\mathrm{ads}}(n) &= h_{\mathrm{ads}}(n) - h_{\mathrm{gas}} \\ &= (H_{\mathrm{wet}}(n) - H_{\mathrm{dry}})/n - h_{\mathrm{gas}} \end{aligned} \quad (1)$$

where $H_{\mathrm{wet}}(n)$ is the enthalpy of the $(TiO_2)_{24}$·nH_2O cluster and $H_{\mathrm{dry}} = H_{\mathrm{wet}}(n=0)$ is the enthalpy of the $(TiO_2)_{24}$ NP alone. h_{gas} is the enthalpy of a gas water molecule, computed with the same parameters employed in the cluster simulations (we use the terms enthalpy and energy interchangeably since the pressure-volume contribution can be neglected). This ideal gas approximation is acceptable for water vapor but might prove less suitable for other molecular gases. Each term in Eq. (1) is obtained from an independent simulation. The surface coverage in terms of number of water molecules per area is determined by the surface area $A = 4\pi r^2$ for the nanoparticle radius $r = 5.5$ Å.

Fig. 8 shows the simulated curves of the (negative) adsorption enthalpies, Δh_{ads}, as functions of water coverage per area, $\rho = n/A$. We have excluded the lowest wetting (corresponding to $n = 1$) which is most prone to sampling errors. The calculated Δh_{ads} is an average over several water molecules at higher surface coverage, but the single-molecule value depends on whether the molecule adsorb at a surface site that favors dissociation (or not). This sampling deficiency can be overcome by longer simulations or several independent simulations with random starting configurations for the water molecule. Either way is computationally expensive. (Note that the basis set superposition errors for the basis employed in our calculations are a few kJ mol^{-1}.[58])

The rutile and anatase NP curves are similar but shifted. The adsorption enthalpies decrease sharply (Δh_{ads} becomes more negative) as $\rho \to 0$, in agreement to experimental data.[37] Δh_{ads} should approach the water enthalpy of vaporization ($\Delta h_{\mathrm{vap}} = -44$ kJ mol^{-1}) when the surface coverage is increased beyond

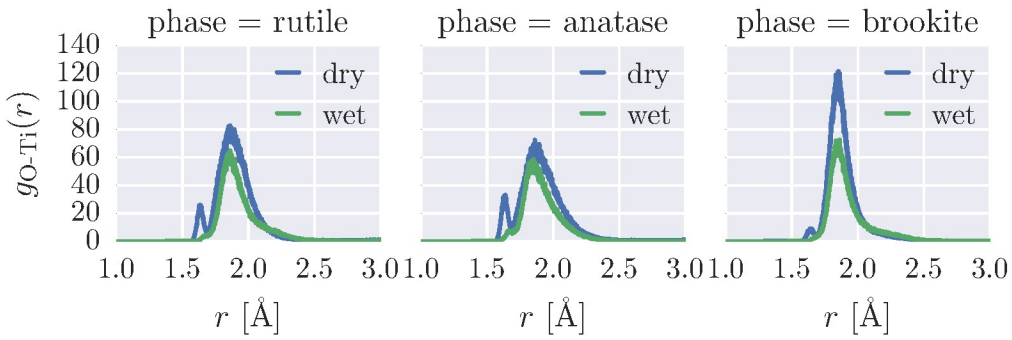

Fig. 5 The radial distribution function (RDF) for O−Ti pairs in the range 1 to 3 Å. The peak at 1.65 Å for dry nanoparticles is due to 1-fold coordinated surface oxygens (see detailed analysis in Fig. 6). Such oxygens are protonated in the wet $(TiO_2)_{24}$-clusters with longer O−Ti bond distances of 1.8 Å. Complete RDFs for all pairs of elements and ranges are found in Fig. ?? in the ESI.

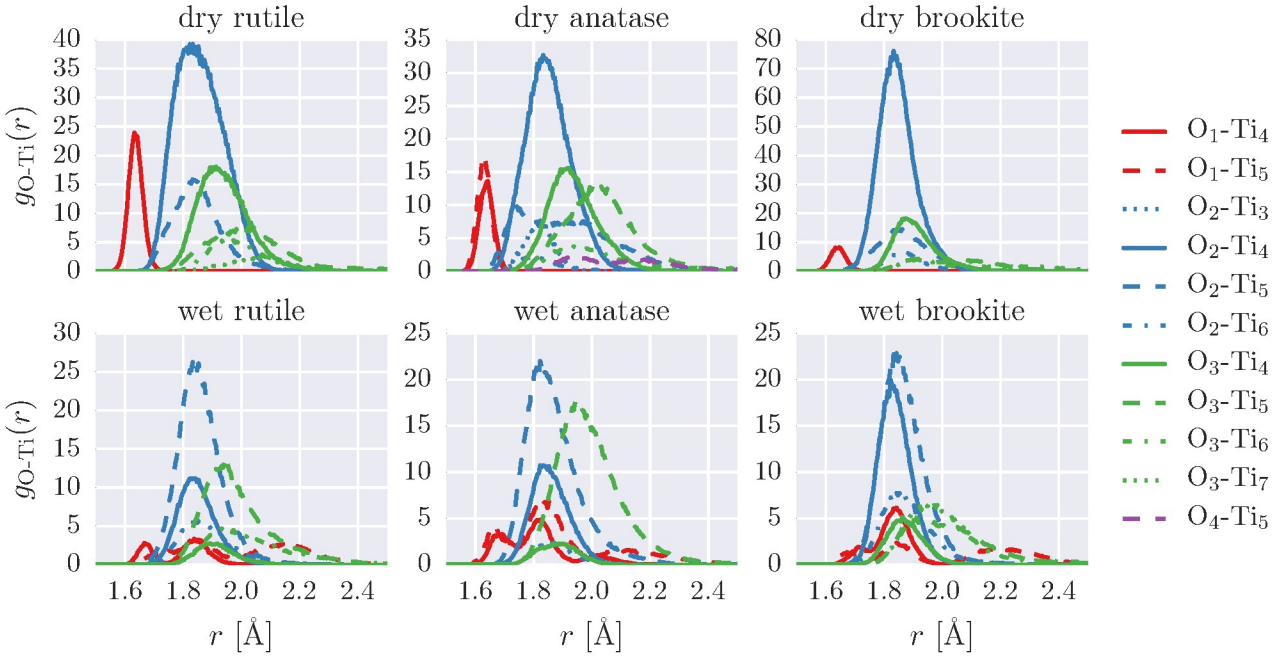

Fig. 6 Radial distribution functions (RDFs) computed for O−Ti pairs based on coordination numbers (CNs). The O−Ti bond distance is 1.6 to 2.2 Å and increases with the CN to an average of 1.95 Å for 3-fold coordinated bulk oxygens. Data corresponding to surface oxygens (one- and two-fold coordinated) are shown in red and blue, and data corresponding to bulk oxygens (three- and four-fold coordinated) are shown in green and purple. Differently coordinated titanium atoms are distinguished by line styles (4-fold = solid, 5-fold = dashed and 6-fold = dashed-dotted). Note the different scales on the vertical axis in the panels.

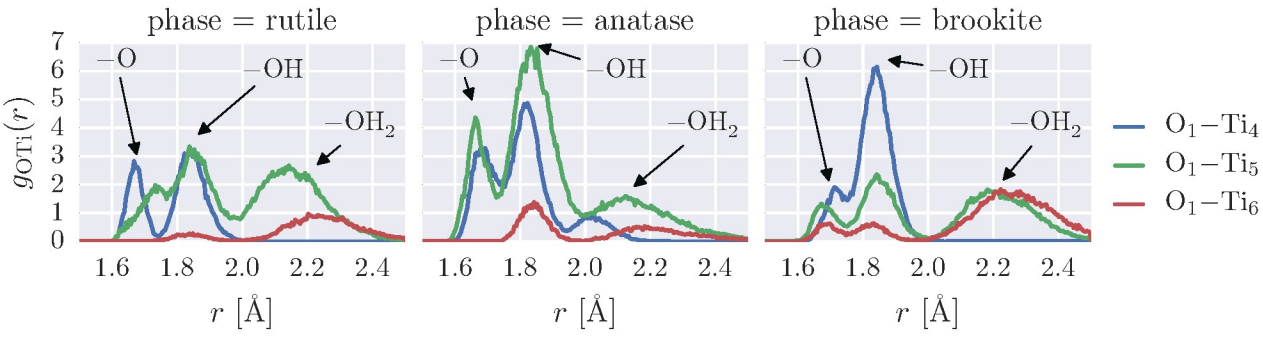

Fig. 7 The radial distribution functions (RDFs) for 1-fold coordinated oxygens on wet nanoparticles ($n = 30$, corresponding to water coverage of 0.08 Å^{-2}). O_1 is coordinated to 4 to 6 titaniums. The peaks correspond to deprotonated oxygens (−O), OH−groups from dissociated waters (−OH), and molecularly adsorbed waters (−OH_2). The distinct peaks show that dissociation and/or molecular adsorption occur at all coordination numbers (CNs), but dissociation is favored at lower CNs.

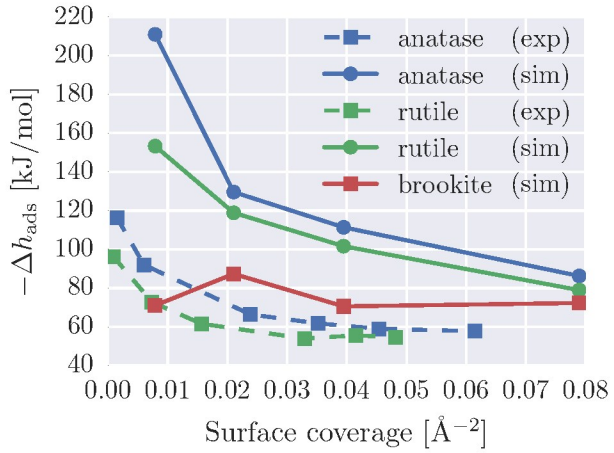

Fig. 8 Calculated adsorption enthalpies (Eq. (1)) for the simulated systems as functions of the surface water coverage. Monolayer coverage corresponds to 0.08 Å^{-2} if a water molecule is assumed to cover the surface area of a disk of radius 2 Å.

the saturation point. Δh_{ads} is (-80 ± 5) kJ mol^{-1} at 0.08 Å^2, the highest coverage in our simulations. The enthalpy of vaporization of BLYP-simulated water with dispersion corrections is[59] (-61.9 ± 3.3) kJ mol^{-1} (Δh_{vap} of water with BLYP without dispersion corrections is (-36.9 ± 2.0) kJ mol^{-1}, in considerably better agreement to experimental data, but by fortuitous cancellation of errors[60]). This value is 25 % lower than the value of Δh_{ads} calculated at 0.08 Å^2, showing that the properties of the adsorbed water monolayer differs from bulk water.

The adsorption curve shapes are in qualitative agreement to experimental data but with more negative Δh_{ads} (up to a factor of 2). This is in line with the known underestimation (overestimation) of the binding energy of water molecules of BLYP without (with) dispersion corrections, due to limitations in the electronic structure model and the neglect of nuclear quantum effects.[59–62] A further limitation in comparing simulated and experimental data is the differing system sizes (10 Å vs. 100 to 300 Å) which makes Δh_{ads} highly sensitive to the surface defects that are common on the surfaces of the small-sized simulation NPs. The experimental trend of anatase being a stronger water binder than rutile[37] is reproduced by the simulations with a gap between the polymorphs that is similar to the experimental data. The adsorption enthalpy for brookite is practically independent of the water content. We are not aware of any experimental adsorption enthalpy curve for brookite but our simulation data suggest weaker water binding on brookite TiO_2 than the other two polymorphs. The photocatalytic activity of brookite has been reported to be similar to, or even higher than, the other polymorphs.[63,64] However, a direct link to experimental adsorption enthalpy is difficult to draw, considering the heterogeneous surface structure of the small-sized nanoparticles studied in the present work and the contribution of chemisorption.

We calculated the heat of immersion, Δh_{imm}, of the monolayer-covered wet nanoparticles, to gain further understanding of the energetics involved in surface wetting. Δh_{imm} is the enthalpy difference per unit area for being adsorbed to the surface compared to being immersed in the bulk, and is calculated using the formula[40]

$$\Delta h_{imm} = (H_{dry} + H_{water} - H_{wet})/A \quad (2)$$

where H_{dry} is the enthalpy of the dry nanoparticle, H_{wet} is the enthalpy of the wet nanoparticle (with $n = 30$), and H_{water} is the total enthalpy of n interacting water molecules. A is the nanoparticle's surface area. We calculated $\Delta h_{imm} =$ 0.64, 0.55 and 0.46 J m^{-2} for the anatase, rutile and brookite nanoparticles, i.e., the same trend as found for the adsorption enthalpies. Experimentally, Δh_{imm} depends strongly on the surface treatment and the amount of water remaining on the dry surfaces[65] but was reported to fall within the range 0.3 to 0.6 J m^{-2}. The less amount of water present on the dry surfaces, the larger the immersion enthalpies grow. The calculated Δh_{imm} are therefore best compared to the upper end of the experimental interval since our "dry" nanoparticle are completely absent of water molecules. The agreement to experimental values is quite good given the uncertainties. Summarizing, the surface energetics shows that the simulation models describe realistic wetting scenarios for ultra-fine TiO_2 NPs.

Water reactivity on small-sized TiO_2 nanoparticles

We measured water reactivity in the simulated systems by calculating coordination numbers (CNs) between elements and then deducing the fraction of dissociated water molecules. Coordinated atoms are within a sphere of radius R from atom i. The number of type B atoms coordinated to atom i of type A is denoted $CN^i_{A\text{-}B}$. Choosing the CN cutoffs to coincide with the first minimum of $g_{TiO}(r)$ and $g_{OH}(r)$ corresponds to $R_{TiO} = 2.5$ Å and $R_{OH} = 1.3$ Å. We then calculated the distributions and moments of $CN^i_{A\text{-}B}$ as described in the Methods section. Fig. **??** in the ESI shows that Ti–O and O–H are the only element pairs that come closer than 2.5 Å (maximum distance for covalent or strong bonding). Ti atoms are then 4- to 6-fold coordinated by oxygens (and denoted Ti_n with $n = \{4,5,6\}$), O atoms are 0- to 3-fold coordinated by titaniums (and denoted O_n with $n = \{0,1,2,3\}$), and H atoms are 1- to 2-fold coordinated by oxygens but never to titaniums. With this terminology, free water molecules are denoted $H_2O_0H_2$ – the oxygen is 0-fold coordinated to titanium and the hydrogens are 2-fold coordinated to oxygen. Molecularly adsorbed waters are subsequently denoted $H_2O_1H_2$, and so on. The TiO_2 bulk coordinations are 3 (oxygen) and 6 (titanium), exactly as in the crystal structures.

Fig. 9 shows the distributions of $CN_{O\text{-}Ti}$ and $CN_{Ti\text{-}O}$ in $(TiO_2)_{24}{\cdot}30H_2O$. The mean of the distributions are 2.2 ± 0.1 and 4.4 ± 0.1 for oxygen and titanium of the dry NPs. The corresponding numbers for the wet NPs are 1.9 ± 0.1 and 4.9 ± 0.1 for oxygen and titanium, respectively. Water oxygens (0-fold coordinated to titanium) were excluded from the calculations of the average CNs of the wet NPs. The decreased O-coordination on wetting is explained by the larger number of O_1 surface atoms – dissociated and molecularly adsorbed waters. Simultaneously, the Ti-coordination is increased from 4.4 to 4.9 because water molecules primarily adsorb at Ti_4 defects (which are then converted to Ti_5-atoms). Zhang *et al.*[34] employed atomistic modeling to interpret

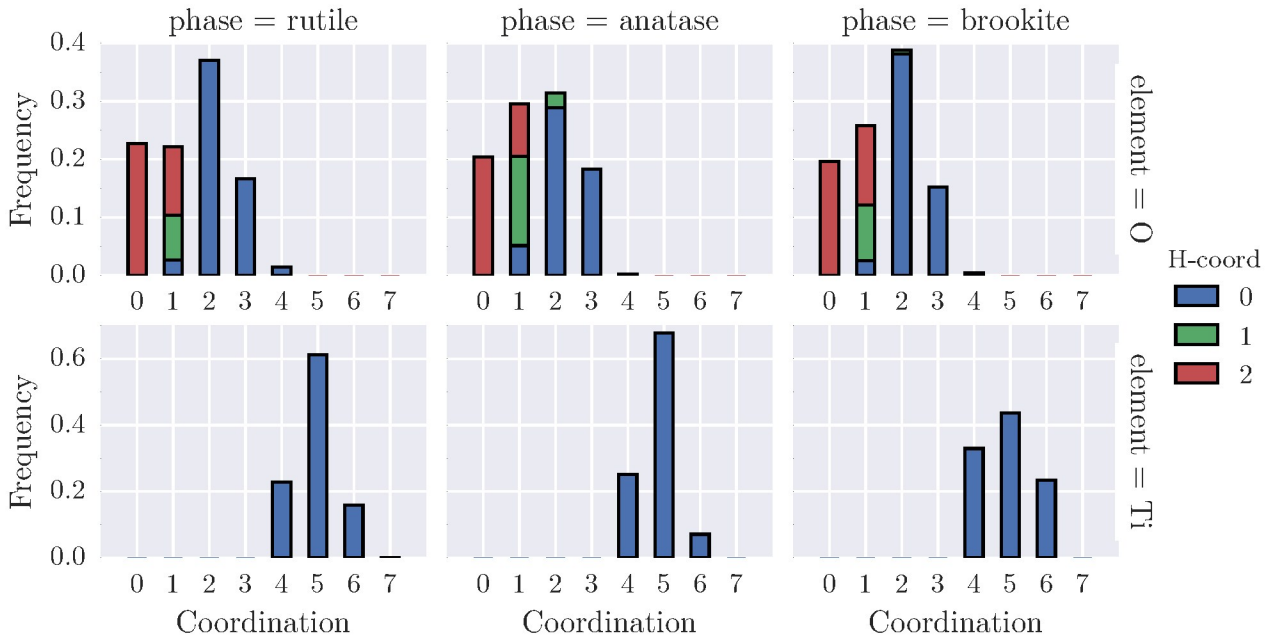

Fig. 9 Coordination number (CN) distributions for O (top panels) and Ti (bottom panels) in the simulated systems, categorized by the accompanying number of coordinated hydrogens. Oxygens that are 0-fold coordinated by titaniums are always 2-fold coordinated by hydrogens, i.e., water molecules. As expected, neither titanium atoms nor bulk oxygens are protonated.

wide-angle x-ray scattering (WAXS) data of amorphous ultrafine titania (dry NPs of sizes 20 to 30 Å) and found anatase-like cores and on average $CN_{Ti-O} = 5.3$ and $CN_{O-Ti} = 2.6$. Similarly, Chen *et al.*[66] reported $CN_{Ti-O} = 5.3$ for 19 Å TiO_2 NPs. Our smaller value (4.4) is expected due to the higher surface-to-bulk ratio in the smaller nanoparticles studied in the present work. There are two major differences between the CN distributions of the dry and the wet nanoparticles (Fig. **??** in the ESI). First, there is a larger proportion of 1-fold coordinated oxygens in the wet nanoparticles due to adsorbed water molecules. Second and more importantly, the proportion of Ti_4 atoms is significantly higher ($\sim 60\,\%$) in the dry nanoparticles than in the wet nanoparticles (25 %). At the same time, Ti_5 increases from 20 to 60 % in the wet NPs, while Ti_6 increases from 5 to 20 %.

The increased Ti coordination in wet TiO_2 is due to adsorption, which occurs both at Ti_4 and Ti_5 defects. But the much larger increase in Ti_5 compared to Ti_6 (after wetting) shows that water molecules adsorb primarily at Ti_4 defects, which are highly reactive compared to Ti_5 sites (see Fig. 7 and the earlier discussion in the text). Fig. 9 shows the number of hydrogens coordination to oxygens that in turn are n-fold coordinated to titaniums. As seen from Fig. 9, titaniums are never protonated. Water oxygens (0-fold coordinated to titaniums) are always associated to exactly two hydrogens. 1-fold coordinated oxygens are only deprotonated in about 10 % of the cases. The rest of the times they are divided more or less evenly between having one hydrogen (OH-group from dissociated water) or two hydrogens (OH_2-group, molecularly adsorbed water). Interestingly, 2-fold coordinated oxygens (Ti–O–Ti bridges on the NP surface) are rarely protonated: 0 % in the rutile simulations, 1.5 % in the brookite simulations, and 8.5 % in the anatase simulations. Their filled electron shells make them inert to protonation, which explains the low reactivity on surfaces with such bridges and low numbers of defects, e.g., rutile (110). We note the fraction of Ti_5 atoms to be lower in wet brookite compared to wet anatase and rutile, even though the distributions are similar in the dry nanoparticles. Water adsorb more frequently on brookite Ti_5 atoms compared to more reactive Ti_4 sites, which are the preferred adsorption sites on the other polymorphs (see Fig. 8).

Fig. 10 shows the water reactivity in the simulated systems, defined as the fraction of dissociated waters compared to the initial number of waters. Fig. **??** in the ESI shows the time evolution of the water reactivity during the course of the simulations. With this definition, the reactivity goes to zero with increasing water content (when bulk waters outweigh surface-adsorbed waters). The reactivity in the $n = 1$-simulations is binary; the single water molecule either splits or stays molecularly adsorbed. Assessing whether this number is zero or one is fraught with the same sampling problems as the adsorption enthalpy at low coverages: the water molecule needs to be sampled homogeneously over the available surface adsorption sites. In any case, the water reactivity differs between the polymorphs. Intriguingly, the reactivity is found to be a concave function of the water content for rutile and anatase, while decreasing monotonously for brookite. The maximum of the function is found at intermediate water contents (8 to 15 water molecules, or 0.02 to 0.04 $Å^{-2}$), which is comparable to the number of available Ti_4 sites (about 12 to 14) on the NPs' surfaces. This level of water coverage would optimize the catalytic reactivity of small-sized nanoparticles used in applications.

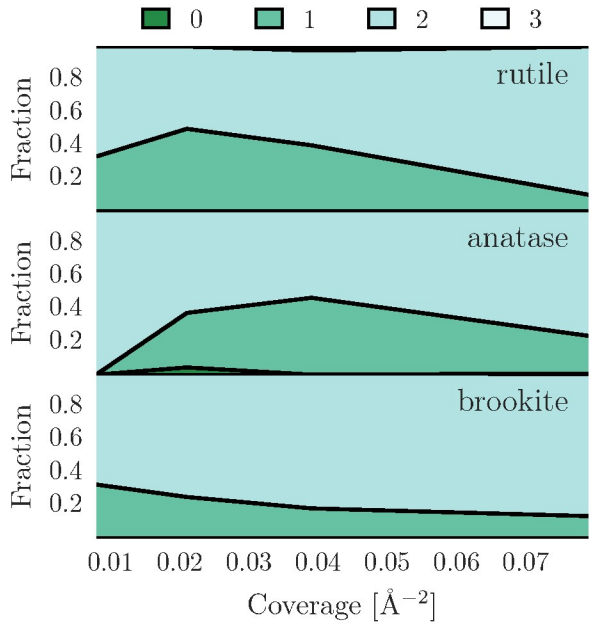

Fig. 10 Water reactivity in the simulated systems (averaged from 15 ps onwards, see Fig. **??** in the ESI), defined as the fraction of dissociated water molecules. The reactivity is maximized when the water coverage is 0.02 to 0.04 Å^{-2} for rutile and anatase, but decreases monotonically with coverage for brookite.

CN	type	q_{Ti} [e]	CN	type	q_O [e]
4	surface	2.07 ± 0.26	0	water	-0.770 ± 0.162
5	surface	2.12 ± 0.24	1	OH	-0.880 ± 0.263
6	bulk	2.170 ± 0.228	2	surface	-1.050 ± 0.208
			3	bulk	-1.180 ± 0.179
			4	bulk	-1.240 ± 0.174

Table 1 Net atomic charges extracted from the simulations using the improved density derived electrostatic and chemical (DDEC) method,[70] grouped by coordination numbers (CNs).

Net atomic charge analysis

Charge transfer (CT) at the TiO_2–water surface could potentially change its catalytic activity and interfacial structure (a fact that is exploited in many biocompatible electronic devices[67,68]). We assessed the role of CT at the TiO_2 NP-water interface by partitioning high-resolution electron densities of the systems according to the net atomic charge (NAC) analysis of Manz and Sholl.[69–71] This state-of-the-art NAC analysis is based on an improved atoms-in-molecules description of the electron density with the aim to assign chemically meaningful fractional charges to each atom in the material. The method optimizes the partial charge distribution to simultaneously reproduce the electrostatic potential and chemical states. The method can be applied both to isolated molecules and to periodic materials; see the Methods Section for more details.

Fig. 11 shows the NAC distributions for titanium and oxygens based on coordination numbers. Each point is a simulation snapshot taken 3 ps apart. We found no discernible differences between the NAC distributions (and consequently in CT) with respect to polymorph. The electron distribution in nano-TiO_2 is insensitive to the long-range repetitions of the ordered structure, but depends on the local coordination (i.e., number of neighbors). The distributions were fitted to Gaussians (solid lines in Fig. 11), and the mean values and standard deviations are summarized in Table 1. Hydrogens were always 1-fold coordinated to oxygens according to a Gaussian NAC distribution (data not shown) with mean and standard deviation $q_H = (0.397 \pm 0.020)e$. In Fig. 11, 0-fold coordinated oxygen are waters, 1-fold coordinated oxygens are dissociated OH–groups or molecularly adsorbed O–H_2 groups (and occasional deprotonated, protruding surface oxygens). 2-fold coordinated oxygens correspond to Ti–O–Ti surface bridges. 3-fold coordinated oxygens and above are bulk atoms. For titanium, 4-fold coordinated are the highly reactive Ti_4 defects while Ti_5 are less reactive surface sites. Bulk titaniums are 6-fold coordinated. There is little CT at the surface for titanium atoms and the NAC distributions are overlapping. In contrast, oxygen CT is substantial, and the NAC distributions for oxygens are comprised of four clearly separated peaks. The partial charge $q_{OW} = (-0.770 \pm 0.162)e$ found for water oxygens (and the corresponding $q_{HW} = (0.39 \pm 0.02)e$ for hydrogens) is in excellent agreement to the typical partial charges employed in simple point charge water models, e.g., the SPC[72] ($q_{OW} = -0.82e$) or TIP3P[73] ($q_{OW} = -0.8340e$) water models. The partial charge becomes more negative with roughly 0.1 to 0.15 e per CN increase. The oxygen charge is 50 % stronger in the metal oxide bulk compared to water. A double peak can be hinted in the NAC distribution of 1-fold coordinated oxygens with splitting due to OH- and OH_2-groups. We ignore this effect in the analysis since the charge difference is rather small ($-0.85\,e$ vs. $-0.95\,e$).

Fig. **??** in the ESI shows that once the water reactivity equilibrates and the surface structure is relaxed, the TiO_2 NP can be described with fixed coordination numbers with respect to the water. To provide a feeling on the charge transfer and polarization in the systems, Fig. **??** in the ESI shows isosurfaces of the electron density plotted on top of the atoms of the equilibrated wet rutile NP. The electron density is depleted around the hydrogens with a corresponding enhancement around the oxygens. The electron density around titanium is less easily disturbed and remains spherical. The polarization contribution of the oxygens is most prevalent. There is a substantial covalent contribution to the Ti–O bond, which is most easily seen by comparing the formal Ti charge ($+4\,e$) to that found in the NPs ($+2.1\,e$).

The NAC analysis shows the profound impact of charge transfer at the TiO_2–water interface. The accompanying polarization difference between the bulk material and the interface will determine the water dipole orientation and hydrogen bonding structure of the surface layer, which in turn modulate the adsorption properties of many biomolecules. The charge fluctuations are about 5 % on hydrogen, 10 % on titanium, and 25 % on oxygen. The Gaussian NAC distributions indicate that fluctuating charge models[74–80] can be advantageous to describe the water interface of TiO_2 NPs in classical models. However, also models with fixed (but CN-dependent) partial charges combined with a predetermined surface structure (number of OH-groups) can yield a good

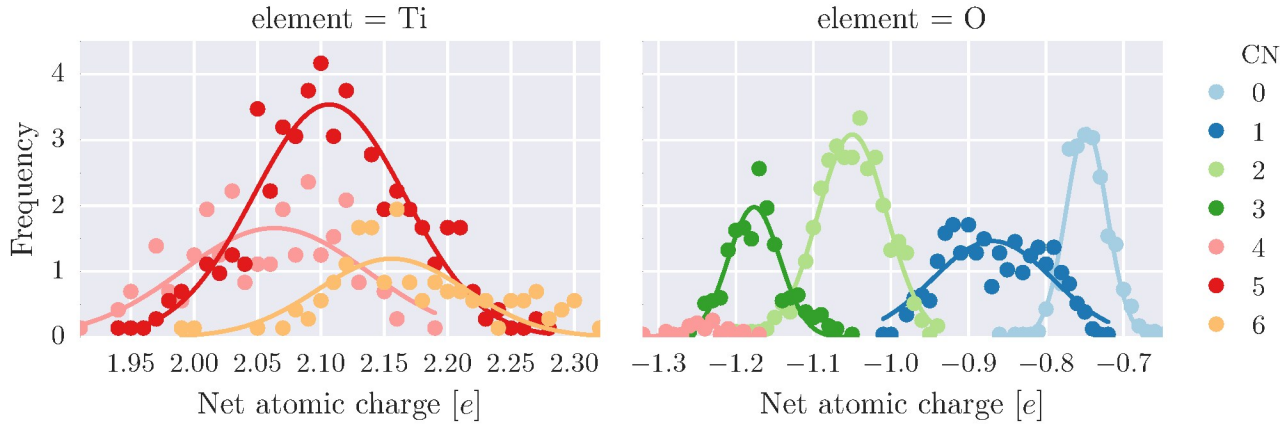

Fig. 11 Net atomic charge (NAC) distributions for Ti and O in nanosized TiO_2, averaged over 10 equilibrated snapshots of each polymorph. The NAC distribution of the polymorphs (rutile, anatase and brookite) are alike and we therefore show averages. Coordination numbers (CNs) refer to O-Ti neighbors.

description of small-sized TiO_2 NPs.

Microscopic description of TiO_2 wetting

Recently, X-ray Photoelectron Spectroscopy (XPS) experiments were performed on hydrated TiO_2 NPs in the size range 20 to 120 nm.[32] Spectra were collected and dry and hydrated NPs were compared. Four water adsorption pathways were suggested based on the collected data: (1) Water dissociation at oxygen vacancies (i.e., surface defects which expose titanium atoms with lower coordination numbers) yields a chemisorbed OH−group and an increasingly hydrophilic NP surface. (2) Molecularly adsorbed waters at bridging, 2-fold coordinated, oxygens. The bridging oxygens could possibly be protonated (e.g., by picking up a proton from another dissociated water molecule). (3) Water physisorbed on OH anchor sites. (4) Water dissociation at Ti_5 atoms which yields Ti−OH surface groups.

Our *ab initio* simulation data can be used to test the adsorption mechanisms proposed by Benkoula *et al.*[32] First, Fig. 7 shows that reactivity is strongly linked to the coordination number. This leads to dissociation in half of the cases (mechanism 1 above) and to strongly adsorbed waters in the other half (resembling mechanism 2). Dissociation yields an increasingly hydrophilic surface. Pure physisorption (mechanism 3) will play a larger role as the water content increases above monolayer coverage. Second, dissociation and molecular adsorption occur to the same extent at surface defects, while at Ti_5 atoms strong physisorption is dominating, which rules out mechanism 4 to have a major role in photocatalytic activity. Ti_4 is more reactive and the main source of dissociation. The NPs studied by Benkoula et. al[32] were significantly larger (20 to 120 nm) than those investigated in the present study ($\sim$ 1 nm). Ti_5 sites are more frequent than Ti_4 sites at the lower surface-to-volume ratio of the larger NPs, while the opposite applies to the small-sized NPs studied here. The accumulated contribution to the experimental signal from Ti_5 dissociation may then dominate the contribution from the more reactive, but fewer in numbers, Ti_4 sites. Further, Fig. 9 shows that bridging oxygens are rarely protonated. Partly this could be to the low water coverage used in the simulations (below and up to monolayer coverage), but also that the 2-fold coordinated oxygen bridges have filled electron shells and are therefore to a larger extent chemically inert. We conclude that the major part of dissociation on TiO_2 NPs occurs at surface defects, and 5-fold coordinated titanium atoms are anchor sites for strong physisorption of water molecules.

Conclusions

We have reported the first *ab initio* calculations on the wetting of small-sized TiO_2 NPs, including thermal fluctuations and real-time water reactivity. We compared structures (RMSDs, RDFs, angle distributions and coordination numbers) and energetics (adsorption and immersion enthalpies) of dry and wet nanoparticles, and assessed the water reactivity and charge transfer at the TiO_2 NP-water interface from first principles.

Our investigations reveal nanosized TiO_2 to be partly amorphous but with remaining features of the bulk morphologies. The high surface-to-volume ratio of small-sized TiO_2 NPs leads to substantial surface relaxation, and the Ti−O bond distance is shown to contract at the surface where the Ti coordination number is lower. Surface oxygens are either 1-fold protonated (OH−group) or 2-fold protonated (OH_2−group, molecularly adsorbed water), and we have shown that water dissociation occurs mainly on surface defects (Ti_4 sites), while molecular adsorption is preferred on Ti_5 sites. Water reactivity was identified to be a concave function of water content on rutile and anatase NPs, while monotonically decreasing on brookite NPs. A maximum was found for intermediate water contents, about 0.02 to 0.04 molecules/Å^2. This is crucial information for controlled engineering of nanosized TiO_2 with optimal water reactivity. Net atomic charge (NAC) analysis showed substantial charge transfer occurring at the water interface, with a clear chemical distinction between water oxygens, surface oxygens, oxygen bridges and bulk TiO_2 oxygens. This data will be central when constructing empirical models of solvated TiO_2 NPs for large-scale simulations of biomolecular adsorption on inorganic nanoparticles. Our simulation data was

used to interpret the XPS experimental data of Benkoula *et al.*[32] We confirmed that surface defects are the primary source of dissociation on TiO_2 NPs, and that 5-fold coordinated titanium atoms play a lesser role for dissociation but instead provide molecular adsorption sites. Further, we ruled out bridging oxygens picking up protons from dissociated waters. It is much more likely that 1-fold coordinated oxygens will be proton acceptors in the presence of surface defects.

We see utmost importance of our results in the construction of small-sized NPs with controlled water reactivity, TiO_2 films with optimal number of defects and/or vacancies, and in the construction of empirical models for large-scale simulations of adsorption to TiO_2 nanoparticles under biological conditions.

Methods

Simulation protocol

The starting configuration for the $(TiO_2)_{24}{\cdot}nH_2O$ nanoclusters were cut out of spheres of the respective polymorph crystal structures – rutile, anatase and brookite. Surface atoms were removed randomly to yield 1:2 stoichiometry for Ti and O atoms. The nanoclusters were placed in the center of a vacuum box with side 22 Å. $n = \{0, 1, 3, 8, 15, 30\}$ water molecules randomly filled this simulation box. The resulting systems were used as starting configurations for the simulations. The $n = 30$ cases are shown in the top panels of Fig. 1.

Born-Oppenheimer *ab initio* molecular dynamics (AIMD) simulations were performed on the 18 systems with the mixed Gaussian and plane wave (GPW) method as implemented in the CP2K code,[50] using an integration time step of 0.5 fs. The electronic structure calculations were done with the QUICKSTEP[81] module using density functional theory (DFT) and the Becke-Lee-Yang-Parr[82,83] (BLYP) generalized gradient approximation (GGA) to the exchange-correlation functional. GGA functionals fail to account for long-range dispersion contributions to the energy.[84] This is particularly troublesome when simulating hydrogen bonding liquids such as water. Therefore, the BLYP functional was augmented with the dispersion corrections (DFT-D3) developed by Grimme *et al.*[85] This combination of functional and dispersion corrections have been shown to best reproduce the properties of liquid water at ambient conditions.[86] Since the melting point of DFT *ab initio* simulated water within the GGA approximation is higher than the experimentally measured value (suggesting an overstructured liquid structure),[87] we kept the temperature at 310 K, i.e., slightly higher than room temperature, using the velocity rescaling thermostat of Bussi, Donadio and Parrinello[88] (BDP) and a relaxation time of 0.1 ps. The temperature equilibrated within 1 ps in all simulated systems. Core electrons were described with the norm-conserving pseudopotentials of Goedecker, Teter and Hütter.[89,90] Valence electrons were expanded as a double-ζ Gaussian basis set with polarization functions (DZVP).[58] A plane wave cutoff at 400 Ry was employed in the calculations, with periodic boundaries in all directions. Each system was simulated for 30 to 35 ps while monitoring the potential energy. Equilibrium was achieved within the first 10 ps (see Fig. **??** in the ESI), and this data was subsequently discarded from further analysis, where not stated otherwise. No appreciable drift was found in the "conserved quantity" of the BDP thermostat.

Numerical analysis

Radial distribution functions. The radial distribution function (RDF) between atom types A and B is defined by

$$g_{\mathrm{AB}}(r) = \frac{V}{N_{\mathrm{A}} N_{\mathrm{B}}} \left\langle \sum_{i \neq j}^{N_{\mathrm{A}}, N_{\mathrm{B}}} \delta\left(r - r_{ij}^{\mathrm{AB}}\right) \right\rangle, \tag{3}$$

where the brackets denote an ensemble average, and r_{ij}^{AB} is the distance between atoms i (atom type A) and j (atom type B). The δ-function is 1 if r_{ij}^{AB} lies within the interval $r + \Delta r$ and 0 otherwise. The bin width was $\Delta r = 0.005$ Å. V is the volume of the simulation box, while N_{A} and N_{B} are the total number of the A and B atom types, respectively.

Coordination numbers. We denote the coordination number (CN) of atom i (of atom type A) to atoms of type B as $\mathrm{CN}_{\mathrm{A\text{-}B}}^{i}$. This quantity is calculated by counting the number of B-type atoms within a cutoff radius R of atom i. The cutoff is chosen to coincide with the first minimum in the RDF for the corresponding A−B atom types (see Figs. 5, Fig. 6 and Fig. **??**), in particular $R_{\mathrm{O-Ti}} = 2.5$ Å and $R_{\mathrm{O-H}} = 1.3$ Å (no H atoms coordinated to Ti atoms). Distributions were calculated by counting $\mathrm{CN}_{\mathrm{A\text{-}B}}^{i}$ over the simulated trajectories (Fig. 9 and Fig. 10).

Root-mean-square-deviation. The root-mean-square-deviation (RMSD) of a set of $3N$ atomic coordinates $\mathbf{x} = (\mathbf{x}_1, \ldots, \mathbf{x}_N)$ with respect to another set of (equally numbered) reference coordinates $\mathbf{x}_{\mathrm{ref}}$ is

$$\mathrm{RMSD}(t) = \sqrt{\frac{1}{N} \sum_{i=1}^{N} ||(\mathbf{R}(t)\mathbf{x}_i(t) - \mathbf{x}_{\mathrm{ref},i}) - \mathbf{b}(t)||^2}, \tag{4}$$

where $\mathbf{x}_i(t)$ are the i:th atom's coordinates at time t, and $\mathbf{x}_{\mathrm{ref},i}$ are the corresponding reference coordinates. The RMSD is calculated by determining the rotation matrix $\mathbf{R}(t)$ and translation vector $\mathbf{b}(t)$ that optimally maps the structure onto the reference coordinates, in the least square sense. The RMSD measures how close the coordinates adhere to the reference structure over the course of the simulation. The RMSD calculation only included atoms that were in the nanoclusters at the start of the simulations (i.e. no waters).

Angles. We use angle distributions to quantify the nanoparticles' structures. Angles were calculated by specifying atom type pairs based on cutoffs (identical to the pair cutoffs used to determine CNs) for atom types Ti, O, and H. We calculated the vectors $\mathbf{r}_{\mathrm{A}_i-\mathrm{B}_j}$ and $\mathbf{r}_{\mathrm{A}_i-\mathrm{C}_k}$ in each simulation frame, with A, B, C being any of Ti, O, and H. The angle $\angle \mathrm{B}_j-\mathrm{A}_i-\mathrm{C}_k$ is calculated by

$$\theta_{jik}^{\mathrm{B-A-C}} = \mathrm{atan2}(|\mathbf{r}_{\mathrm{A_i-B_j}} \times \mathbf{r}_{\mathrm{A}_i-\mathrm{C}_k}|, \mathbf{r}_{\mathrm{A}_i-\mathrm{B}_j} \cdot \mathbf{r}_{\mathrm{A}_i-\mathrm{C}_k}) \tag{5}$$

The function $\mathrm{atan2}(y, x)$ is the arctangent of y/x such that the returned value is in the proper range (0° to 180°). The triplet angles were accumulated (for distributions) or averaged (for averages and moments) over the simulation trajectories.

Net atomic charges. Net atomic charges (NACs) were calculated using the improved atoms-in-molecule charge partitioning scheme of Manz and Scholl.[69–71] Simulation frames were gathered every 3 ps for each polymorph, which sums up to 30 simulation snapshots. The snapshots were energy minimized with a high cutoff of 800 Ry, to generate high-resolution electron densities with grid spacing $\Delta r = 0.0586$ Å for the NAC analysis. The electron density obtained from the 30 ps snapshot of the rutile system is shown in Fig. **??** in the ESI.

Acknowledgements

This research was supported by the European Commission MembraneNanoPart FP7 project, the Carl Trygger Foundation (CTS), and by the Swedish Research Council (Vetenskapsrådet). The simulations were performed on resources provided by the Swedish National Infrastructure for Computing (SNIC) at the National Supercomputer Centre at Linköping University.

References

1 A. Fujishima and K. Honda, *Nature*., 1972, **238**, 37–38.
2 B. O'Regan and M. Grätzel, *Nature*., 1991, **353**, 737–740.
3 U. Diebold, *Surf. Sci. Rep*., 2003, **48**, 53–229.
4 M. Grätzel, *Nature*., 2001, **414**, 338–344.
5 Y. Paz, Z. Luo, L. Rabenberg and A. Heller, *J. Mater. Res*., 1995, **10**, 2842–2848.
6 S. Srivastava, J. P. Thomas, M. A. Rahman, M. Abd-Ellah, M. Mohapatra, D. Pradhan, N. F. Heinig and K. T. Leung, *ACS Nano*, 2014, **8**, 11891–11898.
7 M. Ni, M. K. H. Leung, D. Y. C. Leung and K. Sumathy, *Renew. Sust. Energ. Rev*., 2007, **11**, 401–425.
8 M. D. Newman, M. Stotland and J. I. Ellis, *J. Am. Acad. Dermatol*., 2009, **61**, 685–692.
9 H. J. Johnston, G. R. Hutchison, F. M. Christensen, S. Peters, S. Hankin and V. Stone, *Part. Fibre Toxicol*., 2009, **6**, 33.
10 J. Meng, P. Zhang, F. Zhang, H. Liu, J. Fan, X. Liu, G. Yang, L. Jiang and W. Shutao, *ACS Nano*, 2015, **9**, 9284–9291.
11 S. Wohlfart, S. Gelperina and J. Kreuter, *J. Control. Release*, 2012, **161**, 264–273.
12 T. Wang, H. Jiang, L. Wan, Q. Zhao, T. Jiang, B. Wang and W. Siling, *Acta Biomater*., 2015, **13**, 354–363.
13 F. U. Rehman, C. Zhao, H. Jiang and X. Wang, *Biomater. Sci*., 2016, **4**, 40–54.
14 R. Y. Prasad, K. Wallace, K. M. Daniel, A. H. Tennant, R. M. Zucker, J. Strickland, K. Dreher, A. D. Kligerman, C. F. Blackman and D. M. DeMarini, *ACS Nano*, 2013, **7**, 1929–1942.
15 A. Fujishima, X. Zhang and D. A. Tryk, *Surf. Sci. Rep*., 2008, **63**, 515–582.
16 J. Matthiesen, S. Wendt, J. Ø. Hansen, G. K. H. Madsen, E. Lira, P. Galliker, E. K. Vestergaard, R. Schaub, E. Lægsgaard, B. Hammer and F. Besenbacher, *ACS Nano*, 2009, **3**, 517–526.
17 J. Gao, R. S. Ndong, M. B. Shiflett and N. J. Wagner, *ACS Nano*, 2015, **9**, 3243–3253.
18 M. Mahmoudi, L. Iseult, M. R. Ejtehadi, M. P. Monopoli, F. B. Bombelli and S. Laurent, *Chem. Rev*., 2011, **111**, 5610–5637.
19 P. J. D. Lindan and C. Zhang, *Phys. Rev. B*, 2005, **72**, 075439.
20 F. Allegretti, S. O'Brien, M. Polcik, D. I. Sayago and D. P. Woodruff, *Phys. Rev. Lett*., 2005, **95**, 226104.
21 Y. Li and Y. Gao, *Phys. Rev. Lett*., 2014, **112**, 206101.
22 E. Berardo and M. A. Zwijnenburg, *J. Phys. Chem. C*, 2015, **119**, 13384–13393.
23 F. Allegretti, S. O'Brien, M. Polcik, D. I. Sayago and D. P. Woodruff, *Surf. Sci*., 2006, **600**, 1487–1496.
24 L. E. Walle, A. Borg, P. Uvdal and A. Sandell, *Phys. Rev. B*, 2009, **80**, 235436.
25 D. A. Duncan, F. Allegretti and D. P. Woodruff, *Phys. Rev. B*, 2012, **86**, 045411.
26 H. H. Kristoffersen, J. Ø. Hansen, U. Martinez, Y. Y. Wei, J. Matthiesen, R. Streber, R. Bechstein, E. Lægsgaard, F. Besenbacher, B. Hammer and S. Wendt, *Phys. Rev. Lett*., 2013, **110**, 146101.
27 N. Kumar, P. R. C. Kent, D. J. Wesolowski and J. D. Kubicki, *J. Phys. Chem. C*, 2013, **117**, 23638–23644.
28 D. J. Wesolowski, J. O. Sofo, A. V. Bandura, Z. Zhang, E. Mamontov, M. Předota, N. Kumar, J. D. Kubicki, P. R. C. Kent, L. Vlcek, M. L. Machesky, P. A. Fenter, P. T. Cummings, L. M. Anovitz, A. A. Skelton and J. Rosenqvist, *Phys. Rev. B*, 2012, **85**, 167401.
29 L.-M. Liu, C. Zhang, G. Thornton and A. Michaelides, *Phys. Rev. B*, 2010, **82**, 161415.
30 C. Zhang and P. J. D. Lindan, *J. Chem. Phys*., 2003, **118**, 4620–4630.
31 L. A. Harris and A. A. Quong, *Phys. Rev. Lett*., 2004, **93**, 086105.
32 S. Benkoula, O. Sublemontier, M. Patanen, C. Nicolas, F. Sirotti, A. Naitabdi, F. Gaie-Levrel, E. Antonsson, D. Aureau, F.-X. Ouf, S.-I. Wada, A. Etcheberry, K. Ueda and C. Miron, *Sci. Rep*., 2015, **5**, 15088.
33 L. Zhu, G. Qiang, P. Sun, W. Chen, X. Wang and G. Xue, *ACS Appl. Mater. Interfaces*, 2013, **5**, 10352–10356.
34 H. Zhang, B. Chen, J. F. Banfield and G. A. Waychunas, *Phys. Rev. B*, 2008, **78**, 214106.
35 S.-D. Mo and W. Y. Ching, *Phys. Rev. B*, 1995, **51**, 13023–13032.
36 H. Zhang and J. F. Banfield, *J. Mater. Chem*., 1998, **8**, 2073–2076.
37 V. Bolis, C. Busco, M. Ciarletta, C. Distasi, J. Erriquez, I. Fenoglio, S. Livraghi and S. Morel, *J. Colloid Interface Sci*., 2012, **369**, 28–39.
38 L. Kavan, M. Grätzel, S. E. Gilbert, C. Klemenz and H. J. Scheel, *J. Am. Chem. Soc*., 1996, **118**, 6716–6723.
39 C. Sun, L.-M. Liu, A. Selloni, G. Q. M. Lu and S. C. Smith, *J. Mater. Chem*., 2010, **20**, 10319–10334.
40 E. G. Brandt and A. P. Lyubartsev, *J. Phys. Chem. C*, 2015, **119**, 18110–18125.
41 M. Pastore and F. De Angelis, *ACS Nano*, 2010, **4**, 556–562.
42 F. De Angelis, *Chem. Phys. Lett*., 2010, **493**, 323–327.
43 A. Akbari, J. Hashemi, J. Niskanen, S. Huotari and M. Hakala,

Phys. Chem. Chem. Phys., 2015, **17**, 10849–10855.
44 D. Spagnoli and J. D. Gale, *Nanoscale*, 2012, **4**, 1051–1067.
45 V. N. Koparde and P. T. Cummings, *J. Phys. Chem. C*, 2007, **111**, 6920–6926.
46 V. N. Koparde and P. T. Cummings, *ACS Nano*, 2008, **2**, 1620–1624.
47 P. C. Redfern, P. Zapol, L. A. Curtiss, T. Rajh and M. C. Thurnauer, *J. Phys. Chem. B*, 2003, **107**, 11419–11427.
48 B. Prasai, B. Cai, M. K. Underwood, J. P. Lewis and D. A. Drabold, *J. Mater. Sci*., 2012, **47**, 7515–7521.
49 M. Gałyńska and P. Persson, *Int. J. Quantum Chem*., 2013, **113**, 2611–2620.
50 J. Hutter, M. Iannuzzi, F. Schiffmann and J. VandeVondele, *WIREs. Comput. Mol. Sci*., 2014, **4**, 15–25.
51 V. Blagojevic, Y.-R. Chen, M. Steigerwald, L. Brus and R. A. Friesner, *J. Phys. Chem. C*, 2009, **113**, 19806–19811.
52 J. Zhang, T. F. Hughes, M. Steigerwald, L. Brus and R. A. Friesner, *J. Am. Chem. Soc*., 2012, **134**, 12028–12042.
53 J. Zhang, M. Steigerwald, L. Brus and R. A. Friesner, *Nano Lett*., 2014, **14**, 1785–1789.
54 S. T. Bromley, I. P. R. Moreira, K. M. Neyman and F. Illas, *Chem. Soc. Rev*., 2009, 2657–2670.
55 J. B. Hasted, in *The Physics and Physical Chemistry of Water*, ed. F. Franks, Springer New York, Boston, MA, 1972, ch. Liquid Water: Dielectric Properties, pp. 255–309.
56 D. T. Cromer and K. Herrington, *J. Am. Chem. Soc*., 1955, **77**, 4708–4709.
57 W. H. Baur, *Acta Crystallogr*., 1961, **14**, 214–216.
58 J. VandeVondele and J. Hutter, *J. Chem. Phys*., 2007, **127**, 114105.
59 V. Weber and D. Asthagiri, *J. Chem. Phys*., 2010, **133**, 141101.
60 G. Murdachaew, C. J. Mundy and G. K. Schenter, *J. Chem. Phys*., 2010, **132**, 164102.
61 V. Weber, S. Merchant, P. D. Dixit and D. Asthagiri, *J. Chem. Phys*., 2010, **132**, 204509.
62 M. J. McGrath, J. I. Siepmann, I.-F. W. Kuo, C. J. Mundy, J. VandeVondele, J. Hutter, F. Mohamed and M. Krack, *J. Phys. Chem. A*, 2006, **110**, 640–646.
63 K.-I. Katsumata, Y. Ohno, K. Tomita, T. Taniguchi, N. Matsushita and K. Okada, *ACS Appl. Mater. Interfaces*, 2012, **4**, 4846–4852.
64 T. Shibata, H. Irie, M. Ohmori, A. Nakajima, T. Watanabe and K. Hashimoto, *Phys. Chem. Chem. Phys*., 2004, **6**, 1359–1362.
65 T. Morimoto, M. Nagao and T. Omori, *Bull. Chem. Soc. Jpn*., 1969, **42**, 943–946.
66 L. X. Chen, T. Rajh, W. Jäger, J. Nedeljkovic and M. C. Thurnauer, *J. Synchrotron Radiat*., 1999, **6**, 445–447.
67 T. Tachikawa, T. Yonezawa and T. Majima, *ACS Nano*, 2013, **7**, 263–275.
68 P. Tarakeshwar, J. L. Palma, G. P. Holland, P. Fromme, Y. J. L. and V. Mujica, *J. Phys. Chem. Lett*., 2014, **5**, 3555–3559.
69 T. A. Manz and N. Gabaldon Limas, *ArXiv e-prints*, 2015, 1512.08270.
70 T. A. Manz and D. S. Sholl, *J. Chem. Theory Comput*., 2012, **8**, 2844–2867.
71 T. A. Manz and D. S. Sholl, *J. Chem. Theory Comput*., 2010, **6**, 2455–2468.
72 H. J. C. Berendsen, J. P. M. Postma, W. F. Gunsteren and J. Hermans, in *Intermolecular Forces*, Springer Netherlands, Dordrecht, 1981, ch. Interaction Models for Water in Relation to Protein Hydration, pp. 331–342.
73 W. L. Jorgensen, J. Chandrasekhar, J. D. Madura, R. W. Impey and M. L. Klein, *J. Chem. Phys*., 1983, **79**, 926–935.
74 S. W. Rick, S. J. Stuart and B. J. Berne, *J. Chem. Phys*., 1994, **101**, 6141–6156.
75 S. W. Rick, S. J. Stuart, J. S. Bader and B. J. Berne, *Structure, Fluctuation, and Relaxtion in Solutions*, Elsevier, 1995, vol. 83, pp. 31–40.
76 J. L. Banks, G. A. Kaminski, R. Zhou, D. T. Mainz, B. J. Berne and R. A. Friesner, *J. Chem. Phys*., 1999, **110**, 741–754.
77 S. W. Rick and S. J. Stuart, in *Potentials and Algorithms for Incorporating Polarizability in Computer Simulations*, John Wiley & Sons, Inc., 2003, pp. 89–146.
78 D. V. Matyushov and G. A. Voth, in *New Developments in the Theoretical Description of Charge-Transfer Reactions in Condensed Phases*, John Wiley & Sons, Inc., 2003, pp. 147–210.
79 J. Chen and T. J. Martínez, *Chem. Phys. Lett*., 2007, **438**, 315–320.
80 H. Nakamura, T. Ohto and Y. Nagata, *J. Chem. Theory Comput*., 2013, **9**, 1193–1201.
81 J. VandeVondele, M. Krack, F. Mohamed, M. Parrinello, T. Chassaing and J. Hutter, *Comput. Phys. Commun*., 2005, **167**, 103–128.
82 A. D. Becke, *Phys. Rev. A*, 1988, **38**, 3098–3100.
83 C. Lee, W. Yang and R. G. Parr, *Phys. Rev. B*, 1988, **37**, 785–789.
84 A. J. Cohen, P. Mori-Sánchez and W. Yang, *Chem. Rev*., 2012, **112**, 289–320.
85 S. Grimme, J. Antony, S. Ehrlich and H. Krieg, *J. Chem. Phys*., 2010, **132**, 154104.
86 I.-C. Lin, A. P. Seitsonen, I. Tavernelli and U. Rothlisberger, *J. Chem. Theory Comput*., 2012, **8**, 3902–3910.
87 S. Yoo, X. C. Zeng and S. S. Xantheas, *J. Chem. Phys*., 2009, **130**, 221102.
88 G. Bussi, D. Donadio and M. Parrinello, *J. Chem. Phys*., 2007, **126**, 014101.
89 S. Goedecker, M. Teter and J. Hütter, *Phys. Rev. B*, 1996, **54**, 1703–1710.
90 M. Krack, *Theor. Chem. Acc*., 2005, **114**, 145–152.